13114–13127 *Nucleic Acids Research, 2022, Vol. 50, No. 22* *Published online 9 December 2022*
https://doi.org/10.1093/nar/gkac1162

Salmonella antibacterial Rhs polymorphic toxin inhibits translation through ADP-ribosylation of EF-Tu P-loop

Dukas Jurėnas[1,*], Martial Rey[2], Deborah Byrne[3], Julia Chamot-Rooke[2], Laurent Terradot[4] and Eric Cascales[1,*]

[1]Laboratoire d'Ingénierie des Systèmes Macromoléculaires (LISM), Institut de Microbiologie, Bioénergies et Biotechnologie (IM2B), Aix-Marseille Université, CNRS, UMR 7255, 13009 Marseille, France, [2]Mass Spectrometry for Biology Unit, Université Paris Cité, Institut Pasteur, CNRS, UAR 2024, 75015 Paris, France, [3]Protein Expression Facility, Institut de Microbiologie de la Méditerranée (IMM), Aix-Marseille Université, CNRS, 13009 Marseille, France and [4]Laboratory of Molecular Microbiology and Structural Biochemistry, Institut de Biologie et Chimie des Protéines, Centre National de la Recherche Scientifique, Université de Lyon, UMR 5086, 69367 Lyon, France

Received April 08, 2022; Revised November 11, 2022; Editorial Decision November 12, 2022; Accepted December 07, 2022

ABSTRACT

Rearrangement hot spot (Rhs) proteins are members of the broad family of polymorphic toxins. Polymorphic toxins are modular proteins composed of an N-terminal region that specifies their mode of secretion into the medium or into the target cell, a central delivery module, and a C-terminal domain that has toxic activity. Here, we structurally and functionally characterize the C-terminal toxic domain of the antibacterial Rhs^{main} protein, Tre^{Tu}, which is delivered by the type VI secretion system of *Salmonella enterica* Typhimurium. We show that this domain adopts an ADP-ribosyltransferase fold and inhibits protein synthesis by transferring an ADP-ribose group from NAD$^+$ to the elongation factor Tu (EF-Tu). This modification is specifically placed on the side chain of the conserved D21 residue located on the P-loop of the EF-Tu G-domain. Finally, we demonstrate that the Tri^{Tu} immunity protein neutralizes Tre^{Tu} activity by acting like a lid that closes the catalytic site and traps the NAD$^+$.

GRAPHICAL ABSTRACT

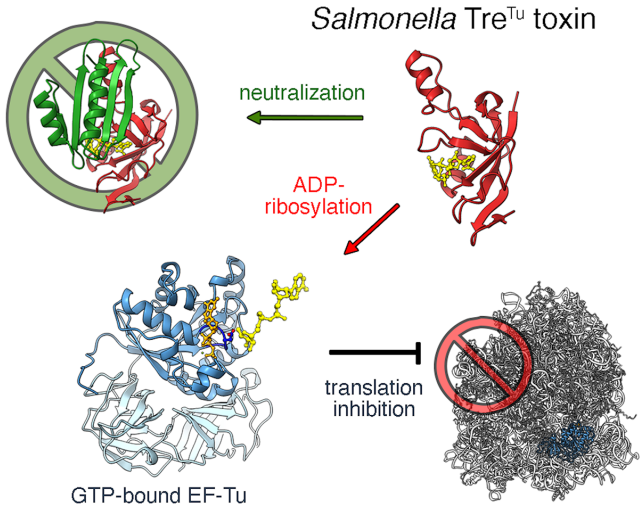

INTRODUCTION

Bacteria produce and secrete toxins to subvert host cells or to destroy microbial rivals (1,2). These toxins are usually secreted through dedicated machineries named secretion systems (3–6). A large family of toxins, collectively known as polymorphic toxins, are modularly organized proteins (7–9): they comprise a highly variable C-terminal domain corresponding to the toxic module fused to an N-terminal region that confers the specificity toward the secretion system (7–9). A broad repertoire of toxin modules has been reported, including toxins with nuclease, protease or ADP-ribosyltransferase (ART) activities (7,9). Interestingly the

*To whom correspondence should be addressed. Tel: +33 491164462; Fax: +33 491712124; Email: cascales@imm.cnrs.fr
Correspondence may also be addressed to Dukas Jurėnas. Email: dukas.jurenas@ulb.be
Present address: Dukas Jurėnas, Cellular and Molecular Microbiology, Faculté des Sciences, Université Libre de Bruxelles, Gosselies, Belgium.

modular architecture of these polymorphic toxins suggests that new toxin modules can be grafted on the N-terminal secretion domain via chromosomal recombination or rearrangements (9). Indeed, Koskiniemi *et al.* have shown that repeated passages of *Salmonella enterica* Typhimurium produce evolved lineages that outcompete the parental strain through the rearrangement and fusion of an untranscribed chromosomal fragment, encoding a toxin domain, to a polymorphic gene (10). This polymorphic toxin, Rhs^{main}, belongs to the family of rearrangement hot spot (Rhs) proteins, which can be associated with various secretion systems. Rhs^{main} is delivered by the type VI secretion system (T6SS) (10), a multiprotein apparatus that uses a contractile mechanism to propel an effector-loaded needle into target cells (11–14). T6SS-associated Rhs proteins have been shown to associate with the T6SS needle tip for transport (15–23).

Rhs proteins form a β-barrel cage-like structure that encapsulates the C-terminal toxin domain (15,17–19). The N-terminal region of these Rhs proteins usually folds as a distinct domain that docks on to the T6SS needle and may include hydrophobic helices likely required for insertion into the membrane of the target cell and hypothetically proposed to support toxin domain translocation into the target cell cytosol (15,17–19). The central cage-like domain of Rhs proteins is delimitated from the N- and C-terminal domains by conserved regions that possess aspartyl protease activity and cleave specific motifs to release the C-terminal toxin domain upon delivery into the target (19,24). While the modular architecture, the structure of Rhs, the mode of delivery and the processing reaction are now well established, only a few toxin domains have been characterized (16,20,25).

In this work, we sought to provide information on the *S. enterica* Typhimurium Rhs^{main} toxin encoded by the *STM0291* gene (GI: 1251810). We show that the C-terminally encoded toxic domain of Rhs^{main} is an antibacterial cytoplasmic-active toxin. The crystal structure of this toxin revealed a typical ART fold with an unusual active site composition. We further show that the toxin inhibits protein synthesis through ADP-ribosylation of the translation elongation factor Tu (EF-Tu), and was therefore named Tre^{Tu} (type VI ribosyltransferase effector targeting EF-Tu). The modification is specifically placed on the conserved D21 residue located in the phosphate binding loop (P-loop) of EF-Tu. Tre^{Tu} activity is neutralized by a specific immunity protein, Tri^{Tu}, that is encoded downstream *rhs*^{main} through complex formation. We then report the crystal structure of the Tre^{Tu}/Tri^{Tu} complex, demonstrating that the immunity protein encloses the NAD^+ and blocks the access to the catalytic pocket.

MATERIALS AND METHODS

Bacterial strains, growth conditions, media and chemicals

Bacterial strains and plasmids used in this study are listed in Supplementary Table S2. Oligonucleotides used for cloning were obtained from Sigma or IDT and are listed in Supplementary Table S3. The purified *S.enterica* Typhimurium LT2 genomic DNA was used as DNA source for polymerase chain reaction (PCR) amplification of the *tre*^{Tu} and *tri*^{Tu} genes. *Escherichia coli* DH5α was used for cloning, and BL21(DE3) was used for protein production and purification. Bacteria were grown in lysogeny broth (LB), with agitation at 37°C. When required, media were supplemented with chloramphenicol (15 μg ml^{-1}) or ampicillin (100 μg ml^{-1}). Gene expression from pBAD33 and pKK vector derivatives was induced by the addition of 0.2% of L-arabinose and 0.5 mM of isopropyl β-D-1-thiogalactopyranoside (IPTG), respectively. Gene expression from pET vector derivatives was induced by the addition of 0.5 mM of IPTG.

Plasmid construction

Genes of interest were amplified by PCR using the Q5 DNA polymerase (NEB) with specific oligonucleotides. PCR products were purified on NucleoSpin Gel and PCR Cleanup columns (Macherey-Nagel), digested with restriction enzymes as recommended by the manufacturer (NEB) and purified before ligation with T4 DNA ligase (NEB). Ligation mixes were transformed into DH5α chemically competent cells, and clones were selected on LB agar plates supplement with the required antibiotics and 1% glucose. Clones were verified by PCR and extracted plasmids (Promega) were verified by sequencing (Eurofins). The *tri*^{Tu} gene was cloned into the EcoRI and HindIII restriction sites of the pKK223-3 vector. A synthetic RBS was introduced into the pBAD33 vector and the resulting pBAD33-rbs vector was used to clone *tre*^{Tu} through the SalI and HindIII restriction sites. The *tre*^{Tu} gene sequence was cloned into the shuttle yeast expression vector pRS416_Gal1 through XbaI and HindIII restriction sites and clones were first selected in *E. coli* DH5α. Tre^{Tu} and EF-Tu amino acid substitution mutants were engineered by site-directed mutagenesis using complementary oligonucleotides (Supplementary Table S3) bearing the desired mutations. The pET-hisTEV-*tre*^{Tu}-*tri*^{Tu} plasmid, encoding 6× His-TEV-tagged Tre^{Tu} and tagless Tri^{Tu}, was obtained by amplifying the pETduet vector with oligonucleotides adding a Tobacco etch virus (TEV) site and restriction enzyme sites. The plasmid fragment and the *tre*^{Tu}-*tri*^{Tu} fragment were digested and ligated into the BmtI and HindIII sites.

Toxicity assays

For toxicity and rescue assays, *E. coli* DH5α cells were co-transformed with pBAD33-rbs and pKK223-3 vectors or their derivatives encoding *tre*^{Tu} and *tri*^{Tu} genes, respectively. Transformants were selected on LB agar plates supplemented with 1% glucose, chloramphenicol (15 μg·ml^{-1}) and ampicillin (100 μg·ml^{-1}). For mutant toxicity assays, *E. coli* DH5α cells were transformed with pBAD33-*tre*^{Tu} or its mutant derivatives and transformants were selected on LB agar plates supplemented with glucose and chloramphenicol. Overnight cultures of transformants were grown in the presence of antibiotics and glucose, serially diluted, and 10 μl drops were spotted on LB agar supplemented with antibiotics and 1% glucose (repression conditions) or 0.2% arabinose (toxin induction conditions) and 0.5 mM IPTG (immunity protein induction conditions). Plates were incubated at 37°C for 16 h.

For toxicity assay in yeasts, the *Saccharomyces cerevisiae* BY4741 yeast strain was transformed with *ura3*-based

pRS416_Gal1 vector and its derivative encoding *tre*^{Tu} gene. Transformants were selected on synthetic dextrose minimal medium (SD) lacking uracil. Overnight cultures of transformants grown in SD media were serially diluted and 10 μl drops were spotted on SD agar and synthetic galactose minimal medium SG for induction. Plates were incubated at 30°C for 3 days.

Protein and complex purification, denaturation and refolding

For Tre^{Tu}-Tri^{Tu} complex purification, the pET-hisTEV-*tre*^{Tu}-*tri*^{Tu} plasmid was transformed into *E. coli* BL21(DE3) cells and selected on LB agar with ampicillin (100 μg·ml^{-1}). Starting from a single colony, the overnight culture was diluted 100-fold into 4 L of LB and grown at 37°C with constant shaking until A_{600} reached 0.8 and then induced with 0.5 mM IPTG. Induction was pursued overnight at 16°C. Cells were then harvested by centrifugation and resuspended in 100 ml of buffer A (50 mM Tris-HCl pH 8.5, 250 mM NaCl, 1 mM Tris-(2-carboxyethyl)phosphine (TCEP)) supplemented with cOmplete™ EDTA-free protease inhibitor mix (Roche). Cells were lysed with a cell disruptor at 4°C, and the total extract was cleared by centrifugation at 49 000 × *g* for 45 min and filtering through a 0.45 μm membrane (Millipore). The protein extract was then loaded on to a 1 ml TALON resin (Takara), and the resin was extensively washed with buffer A. Tagged proteins and complexes were eluted with buffer B (50 mM Tris-HCl pH 8.5, 250 mM NaCl, 1 mM TCEP, 200 mM imidazole). The 6 × His-TEV tag was cleaved with home-purified TEV protease overnight at 4°C. Fractions were pooled, concentrated on to an Amicon spin concentrator (Millipore) and purified by size-exclusion gel filtration chromatography on Superdex 75 10/30 increase column (Cytiva) preequilibrated with gel filtration buffer (50 mM Tris pH 8.5; 250 mM NaCl, 1 mM TCEP). For protein denaturation and refolding, the cells extract containing the 6 × His-TEV-Tre^{Tu}-Tri^{Tu} complex was loaded on to the TALON resin and washed as previously described. After the washing step, the resin was flushed three times with 1-column volume of 8 M urea to unfold the proteins. The flow through, containing the Tri^{Tu} protein, was collected, and the 6 × His-TEV-Tre^{Tu} protein was then eluted with 200 mM imidazole in 7.2 M urea. Denatured proteins were quickly diluted 10-fold with renaturation buffer (50 mM Tris-HCl pH 8.5, 125 mM NaCl, 5% glycerol) and dialyzed two times for 12 h at 4°C in gel filtration buffer. The refolded 6 × His-TEV-Tre^{Tu} protein was cleaved with TEV protease during the dialysis. Proteins were then concentrated and purified by size-exclusion chromatography as described above.

The 6 × His-EF-Tu and its variants were purified from 0.5 L of culture of BL21(DE3) cells freshly transformed with the pET-his-EF-Tu plasmid (26). EF-Tu was purified using the same protocol as the Tre^{Tu}-Tri^{Tu} complex, except from buffer compositions (buffer A: 50 mM HEPES pH 7.5, 40 mM NH_4Cl, 25 mM NaCl, 1 mM TCEP; buffer B: 50 mM HEPES pH 7.5, 40 mM NH_4Cl, 25 mM NaCl, 1 mM TCEP, 200 mM imidazole). Size-exclusion gel filtration chromatography was performed on Superdex 200 increase 10/30 column (Cytiva) in buffer A. For nucleotide removal, the EF-Tu containing fraction was subjected to two rounds of dialysis for 12 h at 4°C in modified buffer A supplemented with 50 mM EDTA. After dialysis, proteins were re-purified in buffer A supplemented with 2 mM $MgCl_2$, and 1 mM of the different nucleotides were added to purified EF-Tu fractions.

Tre^{Tu} and Tre^{Tu}-Tri^{Tu} crystallization, data collection and processing

After purification, tag removal and gel filtration, the Tre^{Tu} domain and the Tre^{Tu}-Tri^{Tu} complex were concentrated to 15–20 mg·ml^{-1} and subjected to sitting-drop vapor diffusion crystallization trials at 20°C. Crystallization drops were set-up in Swissci 96-well 2-drop MRC crystallization plates (Molecular Dimensions) by mixing 0.5 μl of protein with 0.5 μl of precipitant solutions and were equilibrated against 70 μl crystallization screens: Crystal Screen I and II (Hampton Research), LMB, Pact Premier, JCSG plus, MembFac (Molecular Dimensions). For the Tre^{Tu} toxin, the diffraction quality crystals were obtained in 0.2 M $Zn(CH_3COO)_2$, 0.1 M Na-cacodylate pH 6.5, 18% w/v PEG8000. The Tre^{Tu}-Tri^{Tu} complex crystallized in 1 mM $ZnSO_4$, 50 mM HEPES 7.8, 28% PEG600. Crystals were cryo-cooled in a flow of liquid nitrogen. Before cryo-cooling, the Tre^{Tu} crystals were cryo-protected by quickly immersing the crystals into a well solution supplemented with 20% glycerol. Datasets were collected at the PROXIMA-2A (PX2A) beamline (SOLEIL Synchrotron, Gif-sur-Yvette, Paris, France). A high redundancy Tre^{Tu} dataset was collected at the absorption K-edge of Zn (wavelength: 1.27819 Å). The Tre^{Tu} crystals belong to space group P 21 21 21 with unit cell parameters: $a = 51.55$ Å, $b = 66.37$ Å, $c = 67.70$ Å with two molecules per asymmetric unit and diffracted to a resolution of 2.2 Å. The Tre^{Tu} structure was solved by SAD phasing with Autosolve (27), using the anomalous signal of 6 Zn atoms. Tre^{Tu}-Tri^{Tu} crystals diffracted to a resolution of 2.7 Å and belonged to space group P 1 21 1 with unit cell parameters: $a = 58.65$ Å, $b = 94.04$ Å, $c = 61.30$ Å; $\alpha = 90°$, $\beta = 110.07°$, $\gamma = 90°$, with four molecules per asymmetric unit. The structure of Tre^{Tu}-Tri^{Tu} was solved by molecular replacement using Tre^{Tu} crystal structure as a search model with Phaser (28). The Tre^{Tu} and the Tre^{Tu}-Tri^{Tu} structures were built using Autobuild (29) and manual building in Coot (30), refined using Phenix and validated with Molprobity (31). The final Tre^{Tu} model was refined to Rwork/Rfree of 0.19/0.22. The model of the Tre^{Tu}-Tri^{Tu} structure was refined with PDB-REDO (32) to R_{work}/R_{free} of 0.22/0.25. Data collection and refinement statistics are described in Supplementary Table S1. The atomic coordinates and structure factors of Tre^{Tu} and Tre^{Tu}-Tri^{Tu} have been deposited at the Protein Data Bank (PDB) under accession code 7ZHL and 7ZHM, respectively.

Isothermal titration calorimetry (ITC)

Isothermal titration calorimetry (ITC) titrations were carried out with MicroCal PEAQ-ITC machine (Malvern). Before the measurement, the Tre^{Tu} toxin and nucleotide-free EF-Tu were pre-incubated with 2 mM $MgCl_2$ and 10 mM GppNp, and re-purified on Superdex 75 gel filtration column equilibrated with ITC buffer (50 mM Hepes pH 7.5,

40 mM NH_4Cl, 25 mM NaCl, 1 mM TCEP). Before the titrations, all samples were supplemented with 500 μM of NAD^+. The toxin sample concentration in the syringe was 300 μM and EF-Tu sample concentration in the cell was 30 μM. Experiments consisted of 19 injections of 2 μl volumes of toxin into the cell (containing 280 μL of EF-Tu or buffer as controls) with 150 s intervals and a stirring rate of 750 rpm. The titrations were performed at 15°C with reference power set to 10 $\mu cal \cdot s^{-1}$. Titrations were repeated twice and kinetic parameters reflect averages of analysis using one set of sites fitting model.

Mass spectrometry analyses

The purified EF-Tu toxin, after Tre^{Tu} action or not, bound to GTP or GppNp, was buffer-exchanged with 200 mM NH_4CH_3COO using a BioSpin 6 (Bio-Rad).

Intact mass analysis. Samples were nanoelectrosprayed using a TriVersa NanoMate (Advion Biosciences) coupled to an Eclipse mass spectrometer (ThermoFisher Scientific). Data were recorded at 15 K resolution with 10 microscan between 700 and 2000 m/z in protein mode under normal pressure condition. Spectrum were summed and noise thresholded using Peak-by-Peak (SpectroSwiss), then deconvoluted with Unidec (33).

Top-down analysis. The ADP-ribosylated EF-Tu protein bound to GTP was nanoelectrosprayed using a TriVersa NanoMate (Advion Biosciences) coupled to an Eclipse mass spectrometer (ThermoFisher Scientific). Data were recorded at 120 K resolution with 50 microscan in protein mode under normal pressure condition. Charge state 45+ (1016 m/z) was selected and submitted to higher energy collision dissociation (HCD) (NCE 20–40) or EThcD (ETD 1–5; HCD 1–10) fragmentations. For proton transfer charge reduction (PTCR) experiments, all ions generated upon activation were selected and charge-reduced for 25 to 100 ms with a reagent intensity of 7E5. Spectrum with same activation were summed and deconvoluted using Qualbrowser (Extract algorithm). Peaks were assigned with ProSite Lite using 2 ppm error tolerance considering the cysteines free. The modification site was manually assessed by addition of a custom modification of + 541.06, corresponding to the monoisotopic mass of an ADP-ribose addition, on different amino acid.

Bottom-up analysis. About 100 μg of the different EF-Tu preparations were digested at 37°C for 10 min in acid condition (0.1% formic acid [FA]) by 1 μl of Nepenthes digestive fluid as described (34). Digests (1 μg) were analyzed by nanoLC-MS/MS on a QExactive HF mass spectrometer. Generated peptides were separated on a homemade 30-cm C18 column (Kinetex 1.7 μm, XB-C18, Phenomenex) at a 250 $nL.min^{-1}$ flow using a water/acetonitrile (ACN) gradient. After 5 min at 2% solvent B (80% ACN, 0.1% FA), a 60-min linear gradient of solvent B from 8% to 40% was applied followed by a quick ramp to 60% in 5 min. The column was rinsed with a 12 min plate of 95% solvent B followed by an equilibration step of 15 min at 2% solvent B. The scan range of the MS experiment was set between 300 and 1800 m/z. Resolutions were set at 60 K for both MS and MS/MS, AGC at 3E6 for MS and 1E6 for MS/MS. The 10 most intense ions with a charge state of 2 or plus and with a minimum intensity of 9.1E5 were selected with an isolation windows of 1.4 m/z for MS/MS experiment with HCD fragmentation at a normalized collision energy of 29 and then excluded from selection for 8 s.

Bottom-up data analysis. Raw data were searched using PEAKS Studio v7 (Bioinformatics Solutions Inc) with a tolerance of 5 ppm for the precursor and 0.01 Da for the fragments. No enzyme rule was used since the Nepethens digestive fluid is not sequence specific. Two modifications were taken into account: methionine oxidation (+15.99 on M) and ADP-ribose addition (+541.06 Da) with a maximum number of modifications per peptide set to 2. *De novo* data were then searched against *E. coli* EF-Tu sequence. The most comprehensive fragmentation spectra of the EF-Tu peptides identified with an ADP-ribose were selected and manually checked to localize precisely the amino acid residue bearing the modification. Ions with a ribose-phosphate addition (+ 193.998) were specifically tracked as they remain stable after HCD activation.

In vitro transcription-translation assays

Coupled *in vitro* transcription-translation assays were performed with the PURExpress® In vitro Protein synthesis kit (NEB), using DNA template coding for the GFP-strep reporter protein that was amplified using the 5'UTR-GFP and 3'UTR-GFP-strep primers (Supplementary Table S3). When indicated, reactions contained 0.1 mM NAD^+ or 6-biotin-17-NAD^+, 1 μM Tre^{Tu}, 5 μM Tri^{Tu} or Tre^{Tu} pre-incubated with Tri^{Tu} for 5 min at room temperature. Reactions were performed for 2 h at 37°C, and proteins were separated by sodium dodecylsulfate-polyacrylamide gel electrophoresis (SDS-PAGE) or native PAGE, transferred on to nitrocellulose membranes, and GFP-strep was detected by immunoblotting with strep-Tag antibodies (Classic, Bio-Rad).

Effect of Tre^{Tu} toxin on *in vitro* eukaryotic translation was determined by following the production of the luciferase protein in TnT® T7 Quick coupled transcription-translation system (Promega) based on rabbit reticulocyte lysate. Reactions were supplemented with 100 μM NAD^+, and 2 μM of the Tre^{Tu} toxin when indicated. After 2 h of incubation at 30°C, the luciferase activity was measured in microplate reader (Tecan M200 Infinite). About 2.5 μl of reactions were dispensed in black flat bottom 96-well plate (Microfluor 1, Nunc) and covered with 100 μl of buffer (25 mM HEPES pH 7.5, 10 mM $MgCl_2$, 0.5 mM ATP) supplemented with 200 μM of the D-luciferin substrate using a micro-injector. After injection, samples were mixed for 3 s, and luminescence was registered in 6 cycles of 10 s that were integrated for final result. The reactions and measurements were performed in triplicates and averages as well as individual integrated signals were plotted.

In vitro and *ex vivo* biotin-ADP-ribosylation assays

For *ex vivo* biotinylation assays, 50 ml of *E. coli* DH5α cells were grown to late exponential phase and resuspended

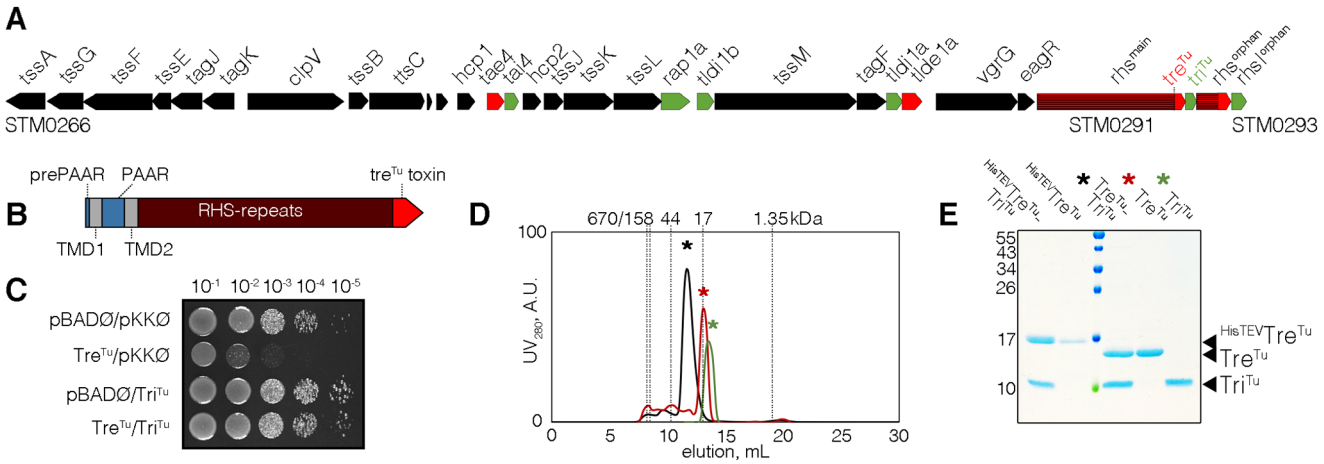

Figure 1. *Salmonella enterica* Rhs^{main} Tre^{Tu} C-terminal domain has antibacterial cytoplasmic-acting activity and is neutralized by Tri^{Tu}. (**A**) Schematic representation of the *S. enterica* Typhimurium LT2 T6SS gene cluster. Genes encoding core and accessory T6SS components are depicted as black arrows. Genes encoding effector protein and domain, and immunity proteins are colored in red and green, respectively. The structural parts of *rhs^{main}* and *rhs^{orphan}* genes are stripped in black and red. (**B**) The schematic representation of the *rhs^{main}*. PAAR domain is colored in blue, transmembrane domains in gray, RHS repeats in brown and Tre^{Tu} toxin domain in red. (**C**) Toxicity assay in the heterologous host *E. coli*. Cultures of *E. coli* cells bearing the empty or Tre^{Tu} toxin-encoded pBAD33rbs and empty or Tri^{Tu} immunity-encoded pKK22.3 plasmids were serially diluted and spotted on LB agar plates supplemented with 0.2% arabinose and 1 mM IPTG to induce expression from pBAD33 and pKK vectors, respectively. (**D**) Gel filtration analyses using Superdex 75 10/30 column. The Tre^{Tu}–Tri^{Tu} complex was purified via the 6× His tag fused to Tre^{Tu}. After TEV protease cleavage, the complex was subjected to size-exclusion chromatography, revealing a unique peak (black peak and black star). In the other assay, the complex bound on the metal-affinity resin was subjected to denaturation by 8 M urea. The two fractions (elution containing Tre^{Tu} and urea wash containing Tri^{Tu}) were then refolded and subjected to size-exclusion chromatography (red and green peaks and stars, respectively). The elution profiles of molecular mass standards indicated on top (in kDa) are shown in dotted lines. (**E**) SDS-PAGE and Coomassie blue staining of the various purified samples: His-TEV-Tre^{Tu}/Tri^{Tu} complex (lane 1), His-TEV-Tre^{Tu} (lane 2), TEV-digested Tre^{Tu}/Tri^{Tu} complex (lane 3), and denaturated/refolded Tre^{Tu} (lane 4) and Tri^{Tu} (lane 5).

in 0.5 ml of phosphate-buffered saline (PBS) buffer. Cells were then disrupted by sonication and 0.1 mM of 6-biotin-17-NAD$^+$ and 1 μM Tre^{Tu} were added when indicated. At different timepoints, aliquots of the reaction were harvested, mixed with 2 × Laemmli loading dye and heated for 5 min at 95°C. For *in vitro* EF-Tu biotinylation assays, 20 μM of purified EF-Tu or its variants were incubated with 0.1 mM of 6-biotin-17-NAD$^+$ and 1 μM Tre^{Tu} and/or 5 μM Tri^{Tu}, as indicated. Reactions were incubated for 15 min at 37°C. All samples from biotinylation assays were separated by SDS-PAGE and transferred on to nitrocellulose membranes. Protein transfer was verified by Ponceau staining, and biotin-ADP-ribosylated proteins were immunodetected with streptavidin-alkaline phosphatase conjugate (Invitrogen).

Accession codes

The final atomic model and coordinates of Tre^{Tu} and of the Tre^{Tu}/Tri^{Tu} complex have been deposited to the Protein Data Bank (PDB) under the accession codes 7ZHL and 7ZHM, respectively. The proteomics data have been deposited to the ProteomeXchange Consortium via the PRIDE partner repository with the dataset identifier PXD033100.

RESULTS

Salmonella Rhs^{main} C-terminal domain, Tre^{Tu}, is a cytoplasmic-acting toxin, which is neutralized by a cognate immunity protein

Salmonella enterica Typhimurium encodes a single functional T6SS gene cluster that comprises all the core elements for the assembly of the secretion apparatus and several antibacterial toxins and their cognate immunity proteins (Figure 1A, (35)). The peptidoglycan-targeting Tae4 and Tlde1 effectors have been recently characterized (36–39). These toxins were suggested to be secreted via the association with the Hcp inner tube protein (37,40). Additionally, it has been previously shown that *S. enterica* Typhimurium gains fitness by secreting T6SS-dependent Rhs toxins for bacterial competition (10). The *S.* Typhimurium T6SS gene cluster encodes a full-length Rhs protein (Rhs^{main}) comprising the N-terminal PAAR domain flanked by putative transmembrane segments, the core composed of RHS repeats, and a C-terminal toxin domain that we named Tre^{Tu} (Figure 1B). This gene is followed by a gene encoding a putative immunity protein (*rhsI^{main}*, hereafter named Tri^{Tu}), and a number of cryptic genes encoding orphan Rhs C-terminal domains and cognate immunities (Rhs^{orphan}/RhsI^{orphan}) (Figure 1A). The regions encoding the orphan Rhs domains have been shown to recombine with *rhs^{main}* to evolve new Rhs effectors (10). However, the cellular activities of these Rhs toxins are not yet known.

To gain insights on the function of the *S. enterica* Typhimurium Rhs^{main} C-terminal Tre^{Tu} extension, the sequence encoding this domain was cloned into the pBAD33 vector. Figure 1C shows that the Tre^{Tu} domain was toxic when produced into the cytoplasm of *E. coli* cells. Tre^{Tu} toxicity was counteracted by the co-expression of the *tri^{Tu}* putative immunity gene (Figure 1C). Pull-down assays show that Tri^{Tu} co-precipitates with Tre^{Tu} (Figure 1D–E). Tre^{Tu} and Tri^{Tu} form a stable protein complex that can only be separated in the presence of 8 M urea (Figure 1D–E). This complex likely comprises one copy of each partner as (i) the intensity of the Tre^{Tu} domain and Tri^{Tu} protein is com-

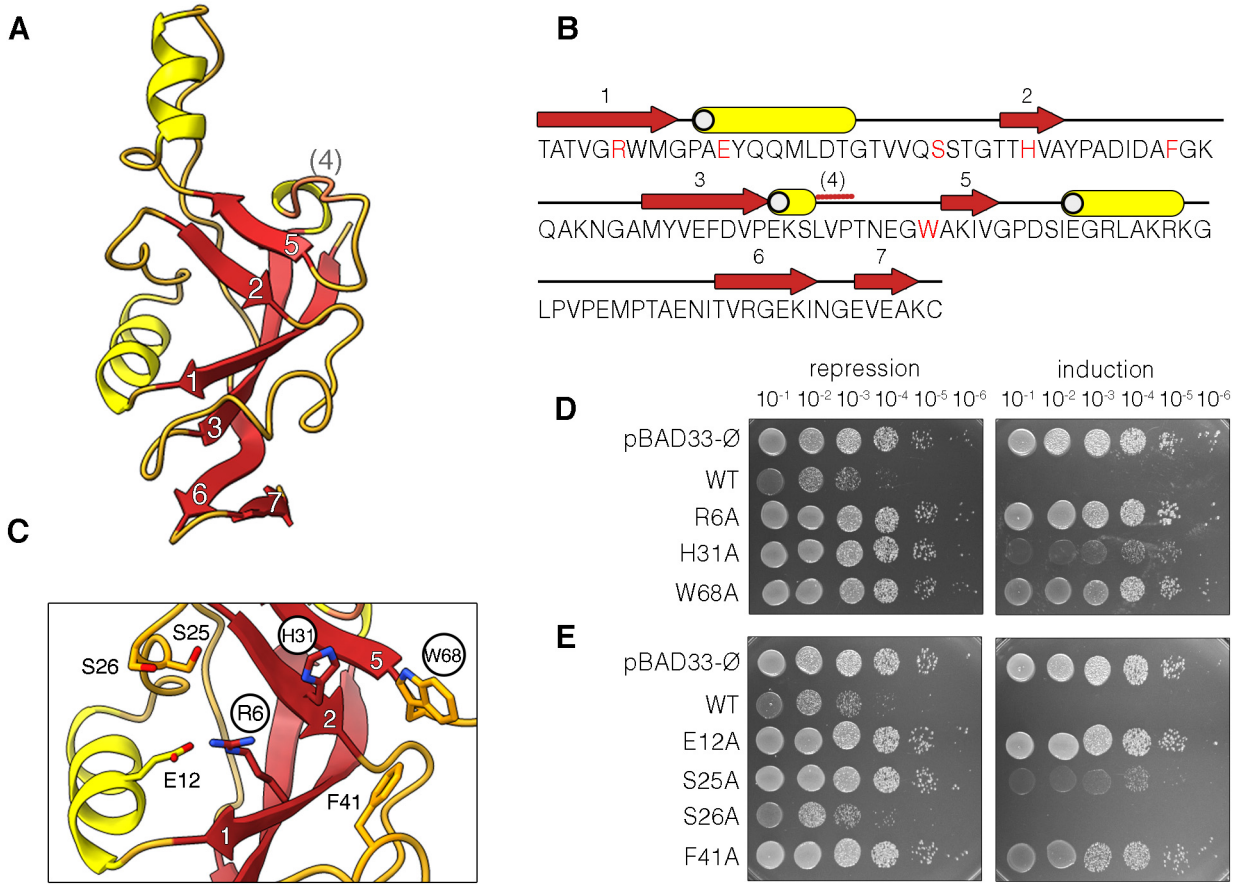

Figure 2. Tre^{Tu} structure. (**A**) Ribbon representation of the *S. enterica* Tre^{Tu} domain. The β -strands, including the pseudo-β-strand β4, are numbered. (**B**) Secondary structures of Tre^{Tu}. The putative residues involved in NAD^+ binding and catalysis are colored by element. (**C**). Magnification of the enzymatic pocket highlighting the residues involved in NAD^+ binding and catalysis. (**D** and **E**) Toxicity assay in the heterologous host *E. coli*. Cultures of *E. coli* cells producing the Tre^{Tu} toxin and its variants from the pBAD33rbs vector were serially diluted and spotted on LB-agar plates supplemented with 1% glucose (repression conditions, left panel) or 0.2% L-arabinose (induction conditions, right panel). Effect of mutations in the putative catalytic triad are shown in (D), and further residues suggested to be involved in NAD^+ binding and catalysis are shown in (E).

parable after Coomassie staining (Figure 1E) and the experimental molecular mass observed by gel filtration (~20 kDa) is similar to the theoretical mass of a 1:1 Tre^{Tu}-Tri^{Tu} complex (23 kDa) (Figure 1D). Taken together these results demonstrate that the *S.* Typhimurium Rhs^{main} C-terminal extension is a cytoplasmic-acting toxin whose activity is neutralized by an immunity protein encoded downstream, likely through stable protein–protein contacts in a 1:1 stoichiometry.

Crystal structure of the Tre^{Tu} domain reveals an ADP-ribosyltransferase fold with an unusual catalytic site

While sequence analysis of *Salmonella* Tre^{Tu} did not provide any information on its potential activity, we pursued its characterization by subjecting the refolded, active (see below), Tre^{Tu} domain to crystallization trials. Tre^{Tu} readily crystallized in a buffer containing zinc acetate, and a diffraction dataset was collected at the Zn K-edge. The structure of Tre^{Tu} was solved by single-wavelength anomalous dispersion (SAD) phasing and refined to a resolution of 2.2 Å (Supplementary Figure S1 and Table S1). The crystal asymmetric unit contained two Tre^{Tu} molecules that show some variability in the C-terminal α-helix and in the loop between β-strands 3 and 5 (which is ordered in the complex between Tre^{Tu} and its immunity protein, Tri^{Tu}, revealing the additional strand β4, see below) that could reflect flexibility of these regions (Supplementary Figure S1C). The Tre^{Tu} monomer consists of a twisted but continuous β-sheet decorated with two major α-helices—one laying on the side of the sheet and another one extending upwards from the sheet (Figure 2A and B). A search for structural homologs using DALI (41) identified a number of mono- and poly-ADP ribosyltransferase (ART) proteins (Supplementary Figure S2). ART proteins transfer the ADP-ribose moiety from the NAD^+ to a target molecule (42,43). While identifying ADP-ribosyltransferases can be difficult solely based on the amino acid sequence (42,44–46), all ARTs comprise a split β-sheet typically composed of six strands in the order of 4–5-2/1–3-6 (42) (Supplementary Figure S2). The *Salmonella* Tre^{Tu} toxin domain displays a similar organization than ARTs, suggesting the position of the toxin active site (Figure 2A and B; Supplementary Figure S2). In ARTs, the split between the two parts of the β-sheet constrains the NAD^+ molecule to the active site composed of a catalytic triad located on strands β1, β2 and β5 (42,47)

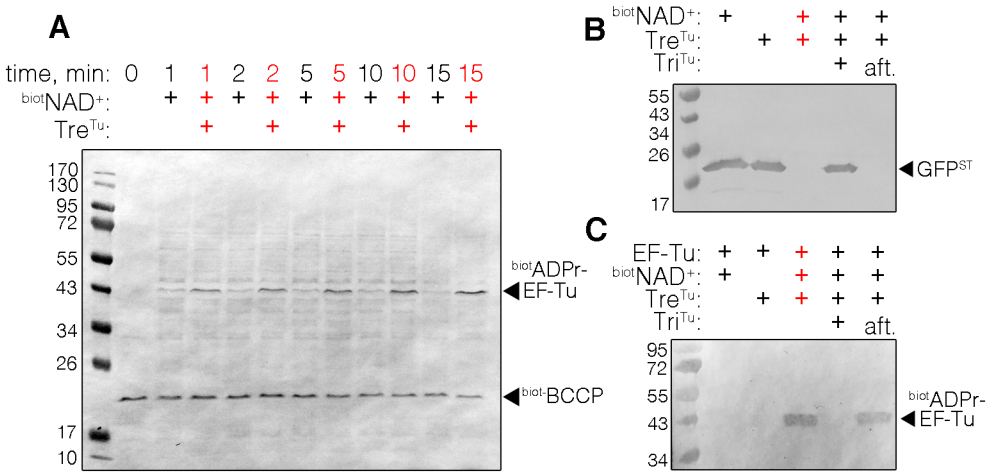

Figure 3. Tre^{Tu} ADP-ribosylates the EF-Tu. (**A**) Time-course ADP-ribosylation assays of cellular extracts of *E. coli* in presence of the Tre^{Tu} toxin and biotin-labeled NAD$^+$. (**B**) Effect of Tre^{Tu} toxin on coupled *in vitro* transcription-translation assays. Synthesis of GFP-strepII protein was followed in the presence of Tre^{Tu} toxin, NAD$^+$ and Tri^{Tu} immunity protein. Synthesized GFP-strepII was then recognized by western blotting with anti-strep antibodies (**C**) ADP-ribosylation of purified his-EF-Tu by the Tre^{Tu} toxin in presence of biotin-labeled NAD$^+$ and of the Tri^{Tu} immunity protein. 'Aft' signifies immunity protein added after the reaction and allowing the reaction to continue.

(Supplementary Figure S2). Based on the composition of these catalytic triads, ARTs are evolutionary clustered into the H-H-h (h being any hydrophobic residue), H-Y-[QED] and R-[ST]-E clades (42). The first active site residue of the triad emerges from the lower surface of strand β1 and this position is occupied by the arginine (R6) in Tre^{Tu}, suggesting that the protein belongs to the R-[ST]-E clade (Figure 2C). However, the upper surface of Tre^{Tu} strands β2 and β5, which should provide the two remaining S/T and E residues of the R-[ST]-E triad, are occupied by histidine H31 and tryptophan W68 instead (Figure 2C). Hence, the Tre^{Tu} active site resembles the less common H-H-h triad found in tRNA 2′-phosphotransferases and CC0527 family enzymes (42). While no other neighboring residues of the corresponding regions seem to be oriented toward the cleft of the split β-sheet, we propose that the active site of the *Salmonella* toxin has an unprecedented hybrid configuration between the R-[ST]-E and H-H-h catalytic triads (Figure 2C). In agreement with this suggestion, alanine substitutions of the R6, H31 and W68 residues inactivated the toxin (Figure 2D). We further tested other residues for which the side chains are oriented toward the same cleft. Notably, substitution of conserved glutamate E12 located on the first α-helix and physically adjacent to the arginine R6 side chain completely inactivated the toxin (Figure 2E). Additionally, a characteristic loop between helix α1 and strand β2 that usually forms a 'wall' of the NAD$^+$-binding pocket (42) contains two serine residues at positions 25 and 26 in Tre^{Tu}. While the S25A substitution impaired toxin activity, the S26A substitution had no effect (Figure 2E). Lastly, substitution of the conserved phenylalanine F41, located on the loop downstream of strand β2 and oriented toward the same cleft, also inactivated Tre^{Tu} toxicity (Figure 2E). Collectively, these results demonstrate that *Salmonella* Rhs^{main} toxic domain displays a characteristic ART fold, with a hybrid or unorthodox catalytic triad (see Discussion).

Tre^{Tu} inhibits translation by ADP-ribosylation of the EF-Tu

Previous T6SS-associated antibacterial ADP-ribosyltransferases have been demonstrated to inhibit cell division or protein synthesis through modification of the FtsZ actin-like protein or of the ribosomal 23S RNA (20,48). To provide information on the Tre^{Tu} cellular target(s), the purified and refolded Tre^{Tu} domain was added to the lysate of susceptible *E. coli* cells in the presence of a biotinylated derivative of NAD$^+$, 6-biotin-17-NAD$^+$. Time-course analysis by SDS-PAGE and blotting with streptavidin–alkaline phosphatase (streptavidin-AP) conjugate revealed an accumulation of a 43-kDa ADP-ribosylated protein in the presence of the Tre^{Tu} toxin (Figure 3A). The biotin-ADP-ribosylated protein target was then enriched on streptavidin beads (Supplementary Figure S3) and identified as the EF-Tu by mass spectrometry. In agreement with this identification, ITC experiments showed that Tre^{Tu} binds EF-Tu with a dissociation constant (K_D) of ∼ 1.7 μM (Supplementary Figure S4). The low affinity suggests that the Tre^{Tu} does not form a stable complex with EF-Tu but rather interacts transiently in order to modify it. EF-Tu being a critical component of the translation machinery, we then tested whether Tre^{Tu} affected protein synthesis. For this, synthesis of a GFP-strep reporter protein was tested in a coupled transcription-translation assay in the absence or presence of Tre^{Tu} and of NAD$^+$. Figure 3B shows that the addition of micromolar amount of the Tre^{Tu} toxin inhibited protein synthesis in the presence of NAD$^+$. When the reaction was supplemented with 6-biotin-17-NAD$^+$, the only ribosylated component in the presence of Tre^{Tu} was EF-Tu (Supplementary Figure S5). This result was confirmed by an *in vitro* assay containing purified EF-Tu, Tre^{Tu} and biotin-NAD$^+$ only (Figure 3C). Addition of Tri^{Tu} in the coupled transcription-translation and *in vitro* assays prevented Tre^{Tu} activity but did not resume protein synthesis and did not reverse EF-Tu modification when

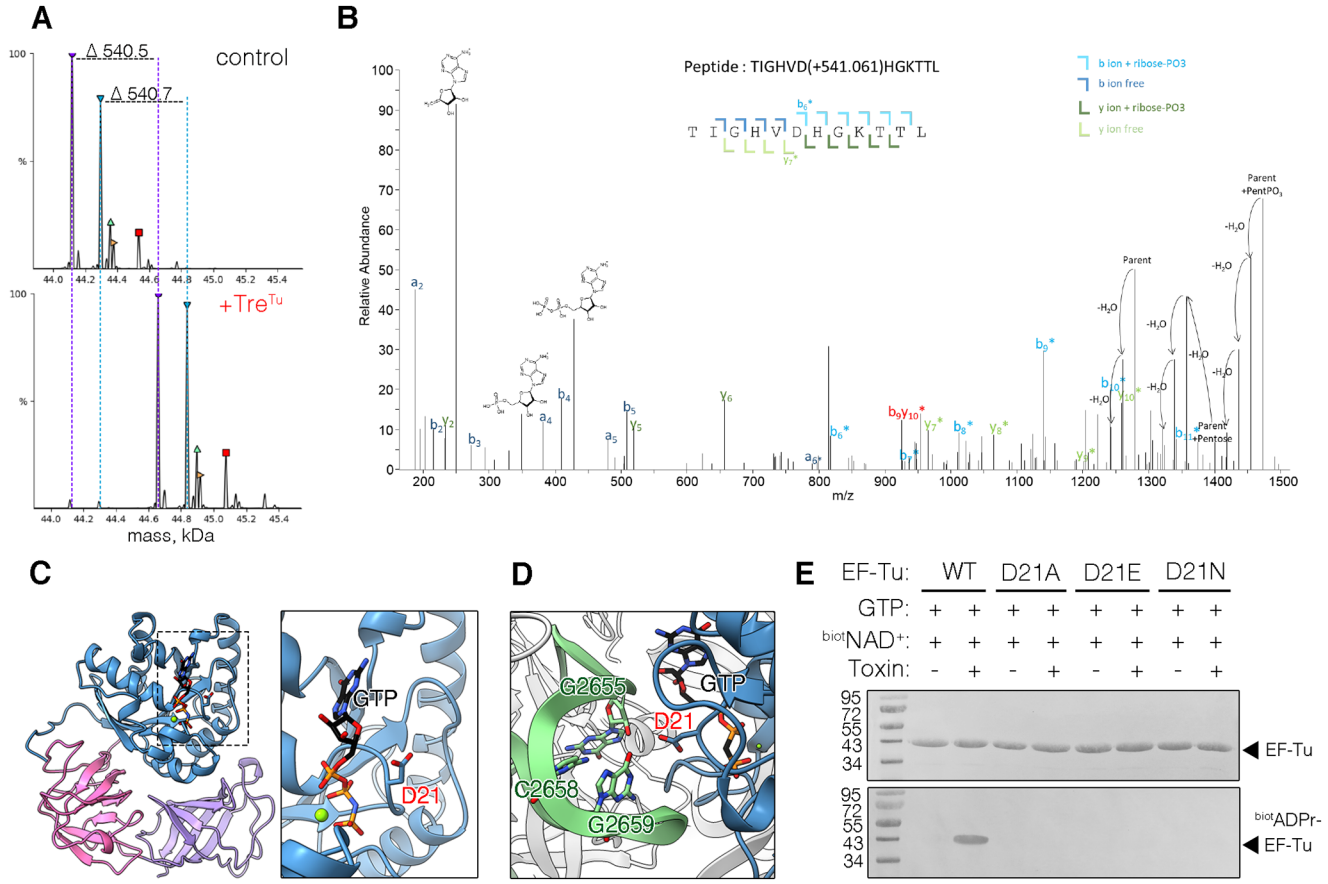

Figure 4. Tre^{Tu} ADP-ribosylates EF-Tu at residue D21. (**A**) Deconvoluted mass spectra of EF-Tu in presence of NAD$^+$ and GTP before (top panel) and after (bottom panel) incubation with Tre^{Tu} toxin. The two major forms correspond to EF-Tu without the initiator methionine (purple) and without the initiator methionine plus an hexose (cyan), respectively. (**B**) Fragmentation spectra of the TIGHVD(ADP-ribose)HGKTTL peptide obtained after HCD activation. b/y ions are labeled respectively in dark blue and dark green. Upon HCD activation, ADP-ribose fragmentation releases the ADP moiety which forms three distinctive ions corresponding from left to right to adenosine, adenosine-phosphate and adenosine diphosphate ions. The ribose-phosphate moiety remains on the peptide fragments, labeled with a star (b*, y* respectively in light blue and light green). Parent peptide can be observed free of modification or with ribose-phosphate addition due to the sensibility of the modification to the activation method. Both forms produce also lots of water loss (labeled '-H2O'). (**C**) EF-Tu structure (blue, PDB:1ob2) highlighting the exposition of residue D21 side chain, which is located on the P-loop of the G domain (domain I). (**D**) In the translating ribosome complex (PDB:4v5l), the side chain of D21 is enclosed in a 23S RNA pocket formed by nucleobases G2655, C2658 and G2659. (**E**) ADP-ribosylation of the wild-type EF-Tu and its D21A, D21E and D21N substitution variants. About 20 μM of purified his-EF-Tu was incubated with GTP, 0.1 μM of biotinylated NAD$^+$ and 1 μM of Tre^{Tu} toxin for 15 min. Proteins were stained by Ponceau rouge after SDS-PAGE and transfer on nitrocellulose membrane (upper panel). The ADP-ribosylation was detected by streptavidin-AP conjugate (lower panel).

added after Tre^{Tu} action (Figure 3B and C), demonstrating that similarly to Tri23 (20), but contrary to Tri1 (48), Tri^{Tu} does not remove the adduct, and is unlikely to have ADP-ribosyl hydrolase activity.

Tre^{Tu} mono-ADP-ribosylates EF-Tu at Asp21

To define the extent of the modification on EF-Tu, the purified EF was incubated with the Tre^{Tu} toxin and NAD$^+$ and then subjected to intact mass spectrometry analyses. Figure 4A shows that all EF-Tu subspecies undergo a ∼541-Da mass increment after incubation with the toxin compared to the control experiment, corresponding to the mass of a single ADP-ribose moiety (541.3 Da). To identify the position of the modification on EF-Tu, ADP-ribosylated EF-Tu was subjected to bottom-up analysis after trypsin digestion. In these conditions, no EF-Tu modification was observed suggesting that the modification is labile and lost during the processing of the sample. To overcome this problem, we performed a bottom-up analysis in acidic conditions after acid digestion of the modified EF-Tu, using *Nepenthes* fluids (34). Several intense peptides containing the modification were manually assigned, limiting the position of the modification to the T^{16}IGHVDHGKTTL^{27} peptide. Looking at the low mass region of the fragmentation data, three specific ions (428.036, 348.070 and 250.093 m/z) arising from the fragmentation of an ADP-ribose moiety and corresponding respectively to an ADP, an AMP and an adenosine could be readily identified, validating the modification identity (Figure 4B). Analysis of all the fragmented peptides carrying the modification localized the modification on the D21 residue (Figure 4B). To identify the position by an independent approach, we analyzed the Tre^{Tu}-modified EF-Tu by top-down MS/MS using electron transfer dissociation (ETD) or HCD (34). Here again, ions corresponding to the fragmentation of the ADP-ribose addi-

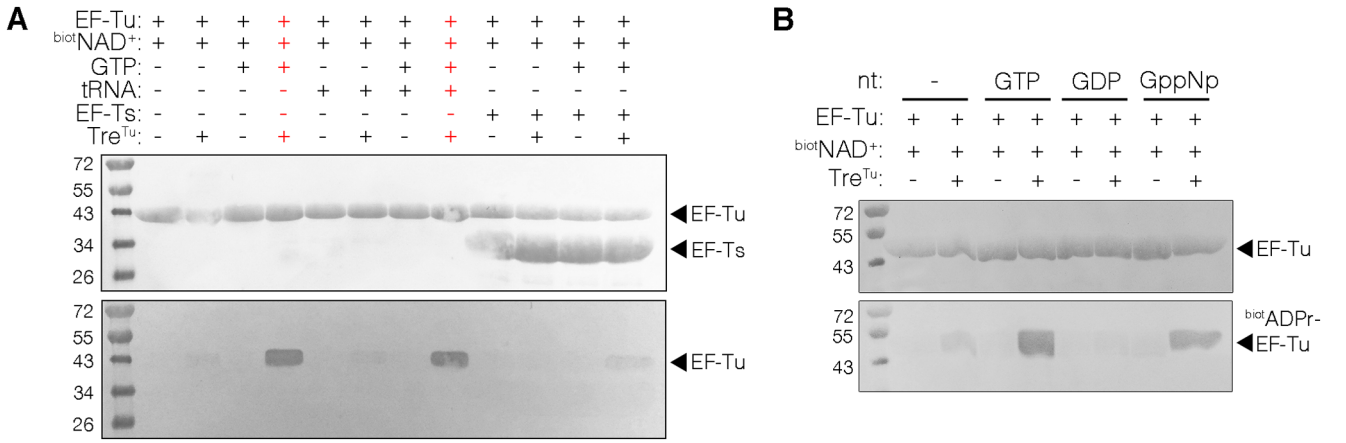

Figure 5. Tre^{Tu} toxin ADP-ribosylates GTP-bound EF-Tu. (**A**) Effect of GTP and/or tRNA or EF-Ts addition on EF-Tu ADP ribosylation by Tre^{Tu}. The composition of each reaction is indicated above the panels. Final concentrations of 20 μM of EF-Tu, 0.1 μM of 6-biotin-17-NAD, 1 μM of Tre^{Tu} toxin, 1 mM of GTP, 100 μM of tRNA or 50 μM of EF-Ts were used for the reactions. (**B**) Effect of the different forms of guanosine phosphate on EF-Tu ADP-ribosylation. Nucleotide-free his-EF-Tu was incubated with the indicated nucleotide and the reactions were performed as previously described. Proteins were stained by Ponceau rouge after SDS-PAGE and transfer on nitrocellulose membrane (upper panels). ADP-ribosylation was detected by streptavidin-AP conjugate (lower panels).

tion were readily identifiable in the low mass region. After deconvolution of the MS^2 spectra and analysis of the top-down data, the modification was localized between residues D21 and T28. To improve the spatial localization of the ADP-ribose addition, we performed PTCR experiment after HCD or ETD fragmentation. Taken together, all experiments provided 205 fragments especially in the N-terminus region where the modification was localized, thus increasing the spatial resolution and narrowing the modification to residue D21 (Supplementary Figure S6). In conclusion, the bottom-up and top-down results unambiguously show that Tre^{Tu} ADP-ribosylates EF-Tu on residue D21. Residue D21 is located within the the P-loop of the EF-Tu G-domain and is part of the signature motif of elongation factors (49) (Figure 4C and D). In order to confirm the position of the modification, EF-Tu substitution variants at D21 (D21A, D21E and D21N) were engineered and purified to homogeneity (Supplementary Figure S7). Upon incubation in the presence of Tre^{Tu} and biotin-NAD^+, none of these variants were biotinylated, demonstrating that Tre^{Tu} specifically targets the EF-Tu D21 side chain (Figure 4E).

Tre^{Tu} ADP-ribosylates the EF-Tu GTP-bound form

The P-loop of EF-Tu binds α- and β-phosphates of GTP or of GDP. The EF-Tu G-domain switch I and II regions sense the presence of the γ-phosphate and undergo conformational changes upon GTP hydrolysis (50). Due to the location of the Tre^{Tu}-mediated adduct and of its exquisite specificity, we further assessed whether the presence of EF-Tu interaction partners—GTP, tRNA and nucleotide exchange factor EF-Ts—would affect the modification. Interestingly, the modification rate increased upon addition of GTP and was not affected by tRNA but largely prevented by the presence of EF-Ts (Figure 5A). To further assess the effect of the presence of nucleotide in the reaction, we produced nucleotide-free EF-Tu and assayed its ADP-ribosylation in the presence of GTP, GDP, or of a non-hydrolysable form of GTP, GppNp. Figure 5B shows that the Tre^{Tu} toxin modified the GTP-bound state of EF-Tu but had no activity on the GDP-bound form. In addition, the modification of the GppNp-bound form of EF-Tu suggested that GTP binding but not GTP-hydrolysis is required for the Tre^{Tu} ART reaction (Figure 5B).

Tri^{Tu} acts like a lid to occlude the active site of Tre^{Tu}

The results presented above demonstrated that Tri^{Tu} neutralizes Tre^{Tu} by forming a protein complex but lacks ADP-ribosyl hydrolase activity. To understand how Tri^{Tu} achieves efficient neutralization of Tre^{Tu}, the purified Tre^{Tu}-Tri^{Tu} complex was subjected to crystallization. The Tre^{Tu}-Tri^{Tu} complex structure was solved by molecular replacement to a 2.7 Å resolution using the Tre^{Tu} structure as a template (Supplementary Table S1). The unit cell of the crystal contained two heterodimers of Tre^{Tu}-Tri^{Tu} (Supplementary Figure S8). The structure of the complex shows that Tri^{Tu} makes extensive contacts with the Tre^{Tu} toxin by binding to the concave β-sheet structure burying a surface of 1100 $Å^2$ (Figure 6A–D). The Tri^{Tu} immunity protein is itself composed of a flat five-stranded antiparallel β-sheet flanked on one side by two α-helices. The Tri^{Tu} β-sheet closely docks against the surface of the Tre^{Tu} toxin and hinders the access to the catalytic site (Figure 6A and B). Strikingly, a NAD^+ molecule is trapped between the toxin and immunity proteins (occupancy of all NAD^+ atoms > 0.9) (Figure 6A–C, Supplementary Figure S9). In agreement with the proposed ART active site described above, the phosphates of NAD^+ form hydrogen bonds with the R6 and S25 side chains of Tre^{Tu} while the NAD^+ riboses associated to the adenine and to the nicotinamide are coordinated by the E12 and H31, and F41 and W68 side chains, respectively (Supplementary Figure S10).

The superimposition of the free and neutralized Tre^{Tu} toxin structures shows they overlap with a root-mean-square deviation (rmsd) of 0.719 Å. Major structural rear-

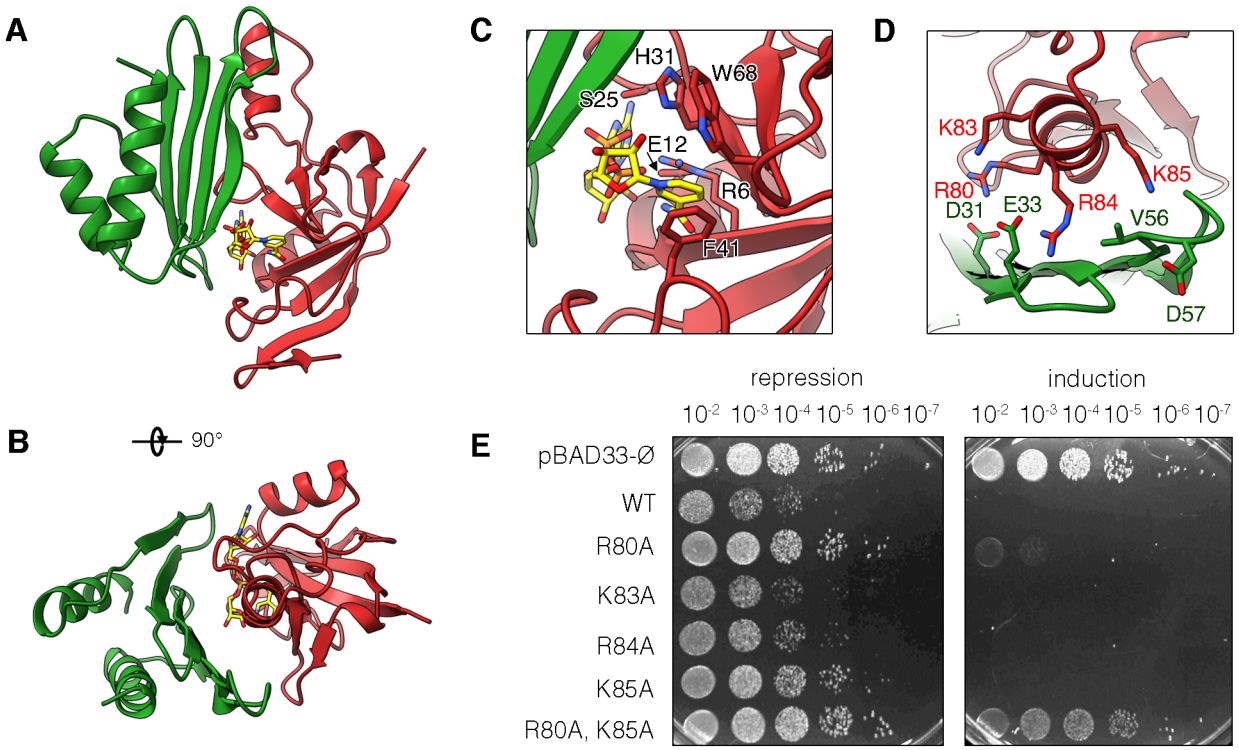

Figure 6. Tri^{Tu} immunity protein neutralizes the Tre^{Tu} toxin blocking its NAD^+ pocket and C-terminal α-helix. (**A,B**) Side (A) and top (B) views of the Tre^{Tu}-Tri^{Tu} complex crystal structure. Tre^{Tu} is shown in red while Tri^{Tu} is shown in green. (**C**) Magnification of the NAD^+ binding pocket, highlighting the NAD^+ molecule (yellow) and the side chains of the putative active site. (**D**) Magnification of the Tre^{Tu} C-terminal helix, highlighting the Tre^{Tu} (red) and Tri^{Tu} (green) residues (colored by element) at the contact site. (**E**) Effect of Tre^{Tu} C-terminal α -helix substitutions on toxicity in the heterologous host *E. coli*. Cultures of *E. coli* cells producing the Tre^{Tu} toxin and its variants from the pBAD33rbs vector were serially diluted and spotted on LB-agar plates supplemented with 1% glucose (repression conditions, left panel) or 0.2% L-arabinose (induction conditions, right panel).

rangements occur on the top part of the split β-sheet and on the C-terminal α3 helix. Notably, the neutralized NAD^+-bound form possesses a folded β4 strand and slightly remodeled β2 and β5 strands (Supplementary Figure S9A). Most importantly, the H31 and W68 side chains that coordinate the NAD^+ adopt different angles (Supplementary Figure S9B). While some of the rearrangements can be attributed to NAD^+ binding, the C-terminal α-helix is located at relatively long distance from the active site. Intriguingly, the Tri^{Tu} immunity protein is positioned slightly upward and the top of its β-sheet is in close contact with the Tre^{Tu} C-terminal α-helix. Moreover, this helix is stabilized by crystallographic dimers and has slightly different conformation in the asymmetric units of both crystals and could thus present flexibility in solution (Supplementary Figures S1 and S8). This helix extends outward of the active site and consists of a series of positively charged residues: R80, K83, R84 and K85 (Figure 6D). Because this α-helix is a unique feature of Tre^{Tu} as compared to other ADP-ribosyltransferases retrieved from DALI search (Supplementary Figure S2), one can speculate that this helix is important for target recognition and binding. Indeed, a non-bias AlphaFold2 (51,52) model of the EF-Tu–Tre^{Tu} complex readily positioned the toxin at the EF-Tu P-loop. Alignment of the modeled toxin with the experimental NAD^+ bound form positions the nicotinamide-associated ribose of NAD^+ close to residue D21 (Supplementary Figure S11A,B). Interestingly, this model suggests that the Tre^{Tu} C-terminal α-helix docks against helix D of the EF-Tu G-domain. More specifically, the side chains of Tre^{Tu} residues R80 and K85 are oriented toward glutamate residues of EF-Tu helix D (Supplementary Figure S11C). To test this model, we introduced alanine substitutions at Tre^{Tu} positions R80, K83, R84 and K85. Figure 6E shows that residues R80 and K85 likely play an important role in Tre^{Tu} function as the toxicity of the R80A and K85A variants was slightly impaired and the double R80-K85A mutant was inactivated (Figure 6E). The AlphaFold2 model of the EF-Tu–Tre^{Tu} complex suggests that the toxin also binds the switch I region of EF-Tu in its GTP-bound conformation (Supplementary Figure S11B). This switch I region drastically changes the conformation and folds backward in the GDP-bound form (53). The loss of contacts with this region might explain the incapacity of Tre^{Tu} to ADP-ribosylate EF-Tu in GDP-bound conformation (Supplementary Figure S11B, Figure 5B).

The exquisite specificity of Tre^{Tu} might also prevent off-target interactions. While the P-loop is highly conserved across all elongation factors (49), none of them were modified *in vivo* or *in vitro*. Further, we found no effect of the toxin towards yeast cells *in vivo* or eukaryotic translation machinery *in vitro* (Supplementary Figure S12). The alignment of the eukaryotic homologue eEF1α1 to the EF-Tu–Tre^{Tu} model suggests that additional eEF1α1 α-helical ele-

ments close to the D17 residue prevent toxin binding (Supplementary Figure S12C).

DISCUSSION

In this work, we provide a functional and structural characterization of the C-terminal extension of the *S. enterica* Typhimurium Rhs^{main} polymorphic toxin, revealing a novel atypical ART enzyme acting on the EF-Tu.

Using a combination of *in vivo* and *in vitro* assays, we provide evidence that Tre^{Tu} inhibits protein synthesis. While structural prediction did not suggest any specific fold, the Tre^{Tu} crystal structure unveiled a typical fold of ADP-ribosyltransferase, comprising a split 6-stranded β-sheet flanked by an α-helix on the convex side.

ADP-ribosyltransferase enzymes transfer the ADP-ribose moiety from the NAD^+ cofactor on to specific targets (43,54). ARTs with toxic functions are rather common (55). They are delivered through various mechanisms and they target diverse substrates. One of the most common targets of ARTs are proteins with G-domains, a universally conserved structure hydrolyzing GTP to switch protein activity between on and off states (49,50). G-domain proteins include translation factors, eukaryotic signaling molecules, such as Ras proteins, or GTP hydrolyzing proteins such as tubulin and the bacterial division component FtsZ (56–58). Indeed, well-characterized bacterial toxins such as the pertussis, cholera and clostridia CTD toxins target eukaryotic G-proteins (59–61), the antibacterial *Serratia proteomaculans* Tre1 toxin targets FtsZ (48) and several ART toxins have been shown to be potent translation inhibitors (20,55,62). Notably, the diphtheria and *P. aeruginosa* ExoA toxins ADP-ribosylate diphtamine residue of the eukaryotic elongation factor, EF-2 (62,63), while we recently reported that the ART-HYD1 family toxin Tre23 from *Photorhabdus* ADP-ribosylates 23S rRNA (20). Protein synthesis inhibition by ADP-ribosylation is thus a common theme, which can be achieved by targeting various translation components. We showed here that Tre^{Tu} arrests protein synthesis by ADP-ribosylating EF-Tu and inhibiting its function. Our biochemical and mass spectrometry results further showed that a single ADP-ribose is transferred on to the D21 residues of the EF-Tu G-domain. The majority of ARTs modifications occur on the NH_2 of the guanidino group of arginine residues, or amide group of glutamine or asparagine side chains. Contrary, the HYE ART clade, comprising the polyADP-ribosyltransferases (PARPs), modifies nucleophilic amino acids, primarily glutamate and aspartate (43,64). While PARPs target multiple sites, to our knowledge, the *S.* Typhimurium Tre^{Tu} toxin characterized here is the first example of an ART that transfers ADP-ribose on a single aspartate. This peculiar characteristic might be explained by its unorthodox catalytic site, which does not fall into the typical RSE, HYE, REH or HHh clade (42). A DALI search showed that the closest structural homologs of Tre^{Tu} are the *Yersinia pseudotuberculosis* CNFγ toxin, which shares a R-E-H triad, but no confirmed ART activity (65,66), and the *Aeropyrum* RNA 2′-phosphotransferase, which possesses a H-H-h triad (67). Previous observations suggested that the orientation of the NAD^+ molecule inside the catalytic pocket is more important than specific residues (42). In agreement with this suggestion, the absence of a third catalytic residue in PARPs does not prevent their activity, although it could be correlated to mono-ADP-ribosylation instead of poly-ADP-ribosylation (64). The crystal structure of Tre^{Tu} bound to NAD^+ demonstrated that the R6, E12, S25, H31, F41 and W68 side chains are involved in NAD^+ coordination (Figure 6), in agreement with the strong impact of the substitution of these residues on Tre^{Tu} activity (Figure 2D and E). We can therefore suggest two different organizations of the catalytic triad, both being different from the typical organizations. Based on the position of catalytic residues in typical ARTs, the Tre^{Tu} active site might be constituted of the R6-H31-W68 triad, which will be a hybrid R-H-h configuration of the R-S-E and H-H-h triads. Alternatively, the triad could be comprised of the typical R6-S25-E12 residues but with an unorthodox positioning.

Tre^{Tu}-mediated EF-Tu modification occurs on a conserved aspartate, D21. The D21 residue is located on the P-loop—a highly conserved motif found in cellular ATPases and GTPases and responsible for coordinating the nucleotide phosphates (49,50). Interestingly, all elongation factors possess a conserved aspartate residue in the center of this motif (49), suggesting an important and specific function of the side chain. It has been hypothesized that EF-Tu D21 could act as a catalyst by contributing to the relative orientation of GTP and Mg^{2+} and to proper GTP hydrolysis (68,69). Indeed, substitutions of the EF-Tu D21 residue have been shown to decrease the GTPase rate of the EF-Tu–tRNA–GTP ternary complexes in the preprogrammed ribosomes (69). Based on these data and on our results demonstrating the addition of an ADP-ribose moiety on the D21 side chain, we propose that the Tre^{Tu} modification may have the same negative effect on EF-Tu GTP hydrolysis, and hence on protein synthesis. Alternatively, the modification of the D21 side chain may have an impact on the proper positioning of EF-Tu on the ribosome. In support of this hypothesis, the EF-Tu structure shows that the D21 side chain points outward from the P-loop and is therefore accessible for ADP-ribosylation by the Tre^{Tu} toxin (Figure 4C). However, when EF-Tu is associated with the ribosome during translation elongation, the D21 side chain is confined into a cavity of the 23S ribosomal RNA formed by nucleobases G2655, C2658 and G2659 (Figure 4D). The ADP-ribose adduct on this side chain would thus likely cause steric clashes preventing proper position of EF-Tu on the ribosome.

Our results demonstrate that the Tre^{Tu} toxin is highly specific to the GTP-bound form of EF-Tu. Discrimination of the two forms likely involves the P-loop and the D21 residue itself. The peptide nitrogen of the D21 residue forms a hydrogen bond with the oxygen of the β-phosphate of the GDP (70), while in the structure of EF-Tu bound to GppNp, the D21 residue binds the β- and γ-imido groups of GppNp. Further, the peptide bond between D21 and the neighboring V20 residue is flipped in the GppNp-bound form as compared to the GDP-bound form (70,71). Taken together, the stereochemistry of the D21 side chain in the different EF-Tu forms may explain why only the GTP-bound form can be targeted by Tre^{Tu}. Binding of GTP by EF-Tu also introduces major rearrangements in regions

known as switches I and II (53). The AlphaFold2 model of Tre^{Tu} bound to EF-Tu suggests toxin contacts with the switch I region in the GTP-bound conformation, which might be necessary to stabilize the interaction (Supplementary Figure S10). Interestingly, nucleotide exchange in EF-Tu was also shown to impact the position of helix D, which connects to nucleotide binding pocket via the loop that recognizes guanine (72). Helix D constitutes the site of contact for the elongation factor Ts (EF-Ts), responsible for nucleotide exchange (73), as well as for the L7/L12 ribosomal subunits (74). The AlphaFold2 model and mutagenesis results suggest that Tre^{Tu} anchors on to the EF-Tu helix D, via its α3 helix, an additional helix that is not a part of the classical ART fold. In this position, the catalytic site of Tre^{Tu} is well oriented to modify the EF-Tu D21 side chain (Supplementary Figure S10). One may hypothesize that Tre^{Tu} also recognizes a specific helix D conformation, to discriminate the EF-Tu forms. Observation that the presence of EF-Ts decreases Tre^{Tu}-mediated EF-Tu modification (Figure 5A) suggests that EF-Ts and Tre^{Tu} compete for the same binding site on EF-Tu and supports the hypothesis that helix D is the main anchoring site for the toxin.

Tre^{Tu} is neutralized by a specific, cognate, immunity protein Tri^{Tu}. Contrary to Tri1, which neutralizes Tre1 and removes the ADP-ribose adduct on the FtsZ target via its ADP-ribose hydrolase activity (48), Tri^{Tu} does not repair the Tre^{Tu}-modified EF-Tu. The crystal structure of the Tre^{Tu}–Tri^{Tu} complex showed that Tri^{Tu} forms a β-lid covering almost all the concave surface of Tre^{Tu}. Tri^{Tu} therefore blocks the access of the NAD^+ substrate to the catalytic site. In addition, the top of the Tri^{Tu} β-lid also interacts with the Tre^{Tu} α3 helix, and hence may prevent the proper interaction between Tre^{Tu} and its target EF-Tu.

In conclusion, we characterized an antibacterial toxin domain, Tre^{Tu}, fused to an Rhs element associated with the *S.* Typhimurium T6SS, highlighting the broad diversity of effectors delivered by this fascinating secretion apparatus. Tre^{Tu} structure–function analysis further unveils that this toxin belongs to an undescribed ART family with an unorthodox catalytic site. Tre^{Tu} transfers an ADP-ribose on a new target, the EF-Tu. The modification occurs on the highly conserved D21 residue, which represents the first example of an ADP-ribose addition on a single aspartate side chain. This exquisite and specific modification likely decreases EF-Tu GTPase activity and prevents proper positioning of EF-Tu on the ribosome, hence inhibiting protein synthesis. Tre^{Tu} therefore represents a novel bacterial translation inhibitor and may thus provide the basis for the rational development of new antibacterials targeting the essential EF-Tu.

DATA AVAILABILITY

All data generated or analyzed in this study are included in the published article and its supplementary information. The final atomic model and coordinates of Tre^{Tu} and of the Tre^{Tu}/Tri^{Tu} complex have been deposited to the Protein Data Bank (PDB) under the accession codes 7ZHL and 7ZHM, respectively. Proteomic data have been deposited to the ProteomeXchange Consortium via the PRIDE partner repository with the dataset identifier PXD033100.

SUPPLEMENTARY DATA

Supplementary Data are available at NAR Online.

ACKNOWLEDGEMENTS

We thank the members of the Cascales laboratory for discussions and support; Maïalène Chabalier, Sophie Du Crest, Moly Ba, Isabelle Bringer, Annick Brun, Audrey Gozzi and Mathilde Valade (LISM, Marseille) for technical support; Pascal Mansuelle and Régine Lebrun (IMM, Proteomic facility) for EF-Tu identification by mass spectrometry; Jérémy Guérin (IBCP, now at Calixar, Lyon) for pilot structural analyses; and the Synchrotron facility (Soleil Saint-Aubin—Proxima2 beamline) for beamline allocation and assistance during data acquisition.
Author contributions: D.J. and E.C. designed research. D.J. and M.R. performed research. D.B., L.T., J.C.R. and E.C. provided tools. D.J., M.R., D.B., J.C.R., L.T. and E.C. analyzed the data. D.J. and E.C. wrote the manuscript with contributions from all authors.

FUNDING

Centre National de la Recherche Scientifique; Horizon 2020 Framework Programme [82383]; Fondation Bettencourt Schueller; Agence Nationale de la Recherche [ANR-10-LABX-62-IBEID, ANR-17-CE11-0039 and ANR-20-CE11-0017]; Fondation pour la Recherche Médicale [DEQ20180339165 and SPF201809007142]. Funding for open access charge: Agence Nationale de la Recherche [ANR-20-CE11-0017].
Conflict of interest statement. None declared.

REFERENCES

1. Lemichez,E., Popoff,M.R. and Satchell,K.J.F. (2020) Cellular microbiology: bacterial toxin interference drives understanding of eukaryotic cell function. *Cell Microbiol.*, **22**, e13178.
2. Peterson,S.B., Bertolli,S.K. and Mougous,J.D. (2020) The central role of interbacterial antagonism in bacterial life. *Curr. Biol.*, **30**, R1203–R1214.
3. Backert,S. and Meyer,T.F. (2006) Type IV secretion systems and their effectors in bacterial pathogenesis. *Curr. Opin. Microbiol.*, **9**, 207–217.
4. Geissler,B. (2012) Bacterial toxin effector-membrane targeting: outside in, then back again. *Front. Cell. Infect. Microbiol.*, **2**, 75.
5. Jurėnas,D. and Journet,L. (2021) Activity, delivery, and diversity of type VI secretion effectors. *Mol. Microbiol*, **115**, 383–394.
6. Roderer,D. and Raunser,S. (2019) Tc toxin complexes: assembly, membrane permeation, and protein translocation. *Annu. Rev. Microbiol.*, **73**, 247–265.
7. Jamet,A. and Nassif,X. (2015) New players in the toxin field: polymorphic toxin systems in bacteria. *mBio*, **6**, e00285–e00215.
8. Ruhe,Z.C., Low,D.A. and Hayes,C.S. (2020) Polymorphic toxins and their immunity proteins: diversity, evolution, and mechanisms of delivery. *Annu. Rev. Microbiol.*, **74**, 497–520.
9. Zhang,D., de Souza,R.F., Anantharaman,V., Iyer,L.M. and Aravind,L. (2012) Polymorphic toxin systems: comprehensive characterization of trafficking modes, processing, mechanisms of action, immunity and ecology using comparative genomics. *Biol. Direct*, **7**, 18.
10. Koskiniemi,S., Garza-Sánchez,F., Sandegren,L., Webb,J.S., Braaten,B.A., Poole,S.J., Andersson,D.I., Hayes,C.S. and Low,D.A. (2014) Selection of orphan Rhs toxin expression in evolved *Salmonella enterica* serovar Typhimurium. *PLoS Genet.*, **10**, e1004255.

11. Brackmann,M., Nazarov,S., Wang,J. and Basler,M. (2017) Using force to punch holes: mechanics of contractile nanomachines. *Trends Cell Biol.*, **27**, 623–632.
12. Cherrak,Y., Flaugnatti,N., Durand,E., Journet,L. and Cascales,E. (2019) Structure and activity of the type VI secretion system. *Microbiol. Spectr.*, **7**, PSIB-0031-2019.
13. Coulthurst,S. (2019) The Type VI secretion system: a versatile bacterial weapon. *Microbiology (Reading)*, **165**, 503–515.
14. Wang,J., Brodmann,M. and Basler,M. (2019) Assembly and subcellular localization of bacterial type VI secretion systems. *Annu. Rev. Microbiol.*, **73**, 621–638.
15. Ahmad,S., Tsang,K.K., Sachar,K., Quentin,D., Tashin,T.M., Bullen,N.P., Raunser,S., McArthur,A.G., Prehna,G. and Whitney,J.C. (2020) Structural basis for effector transmembrane domain recognition by type VI secretion system chaperones. *Elife*, **9**, e62816.
16. Alcoforado Diniz,J. and Coulthurst,S.J. (2015) Intraspecies competition in Serratia marcescens is mediated by type VI-secreted Rhs effectors and a conserved effector-associated accessory protein. *J. Bacteriol.*, **197**, 2350–2360.
17. Donato,S.L., Beck,C.M., Garza-Sánchez,F., Jensen,S.J., Ruhe,Z.C., Cunningham,D.A., Singleton,I., Low,D.A. and Hayes,C.S. (2020) The β-encapsulation cage of rearrangement hotspot (Rhs) effectors is required for type VI secretion. *Proc. Natl Acad. Sci. USA*, **117**, 33540–33548.
18. Günther,P., Quentin,D., Ahmad,S., Sachar,K., Gatsogiannis,C., Whitney,J.C. and Raunser,S. (2022) Structure of a bacterial Rhs effector exported by the type VI secretion system. *PLoS Pathog.*, **18**, e1010182.
19. Jurėnas,D., Rosa,L.T., Rey,M., Chamot-Rooke,J., Fronzes,R. and Cascales,E. (2021) Mounting, structure and autocleavage of a type VI secretion-associated Rhs polymorphic toxin. *Nat. Commun.*, **12**, 6998.
20. Jurėnas,D., Payelleville,A., Roghanian,M., Turnbull,K.J., Givaudan,A., Brillard,J., Hauryliuk,V. and Cascales,E. (2021) Photorhabdus antibacterial Rhs polymorphic toxin inhibits translation through ADP-ribosylation of 23S ribosomal RNA. *Nucleic Acids Res.*, **49**, 8384–8395.
21. Koskiniemi,S., Lamoureux,J.G., Nikolakakis,K.C., t'Kint de Roodenbeke,C., Kaplan,M.D., Low,D.A. and Hayes,C.S. (2013) Rhs proteins from diverse bacteria mediate intercellular competition. *Proc. Natl Acad. Sci. USA*, **110**, 7032–7037.
22. Ma,J., Sun,M., Dong,W., Pan,Z., Lu,C. and Yao,H. (2017) PAAR-Rhs proteins harbor various C-terminal toxins to diversify the antibacterial pathways of type VI secretion systems. *Environ. Microbiol.*, **19**, 345–360.
23. Zheng,H.-Y., Yang,L. and Dong,T. (2021) More than just a spearhead: diverse functions of PAAR for assembly and delivery of toxins of the contractile injection systems. *Msystems*, **6**, e0138621.
24. Pei,T.-T., Li,H., Liang,X., Wang,Z.-H., Liu,G., Wu,L.-L., Kim,H., Xie,Z., Yu,M., Lin,S. *et al.* (2020) Intramolecular chaperone-mediated secretion of an Rhs effector toxin by a type VI secretion system. *Nat. Commun.*, **11**, 1865.
25. Mok,B.Y., de Moraes,M.H., Zeng,J., Bosch,D.E., Kotrys,A.V., Raguram,A., Hsu,F., Radey,M.C., Peterson,S.B., Mootha,V.K. *et al.* (2020) A bacterial cytidine deaminase toxin enables CRISPR-free mitochondrial base editing. *Nature*, **583**, 631–637.
26. Talavera,A., Hendrix,J., Versées,W., Jurėnas,D., Van Nerom,K., Vandenberk,N., Singh,R.K., Konijnenberg,A., De Gieter,S., Castro-Roa,D. *et al.* (2018) Phosphorylation decelerates conformational dynamics in bacterial translation elongation factors. *Sci. Adv.*, **4**, eaap9714.
27. Liebschner,D., Afonine,P.V., Baker,M.L., Bunkóczi,G., Chen,V.B., Croll,T.I., Hintze,B., Hung,L.W., Jain,S., McCoy,A.J. *et al.* (2019) Macromolecular structure determination using X-rays, neutrons and electrons: recent developments in Phenix. *Acta Crystallogr. D Struct. Biol.*, **75**, 861–877.
28. McCoy,A.J., Grosse-Kunstleve,R.W., Adams,P.D., Winn,M.D., Storoni,L.C. and Read,R.J. (2007) Phaser crystallographic software. *J. Appl. Crystallogr*, **40**, 658–674.
29. Terwilliger,T.C., Grosse-Kunstleve,R.W., Afonine,P.V., Moriarty,N.W., Zwart,P.H., Hung,L.W., Read,R.J. and Adams,P.D. (2008) Iterative model building, structure refinement and density modification with the PHENIX AutoBuild wizard. *Acta Crystallogr. D Biol. Crystallogr*, **64**, 61–69.
30. Emsley,P. and Cowtan,K. (2004) Coot: model-building tools for molecular graphics. *Acta Crystallogr. D Biol. Crystallogr*, **60**, 2126–2132.
31. Williams,C.J., Headd,J.J., Moriarty,N.W., Prisant,M.G., Videau,L.L., Deis,L.N., Verma,V., Keedy,D.A., Hintze,B.J., Chen,V.B. *et al.* (2018) MolProbity: more and better reference data for improved all-atom structure validation. *Protein Sci.*, **27**, 293–315.
32. Joosten,R.P., Long,F., Murshudov,G.N. and Perrakis,A. (2014) The PDB_REDO server for macromolecular structure model optimization. *IUCrJ*, **1**, 213–220.
33. Marty,M.T., Baldwin,A.J., Marklund,E.G., Hochberg,G.K.A., Benesch,J.L.P. and Robinson,C.V. (2015) Bayesian deconvolution of mass and ion mobility spectra: from binary interactions to polydisperse ensembles. *Anal. Chem.*, **87**, 4370–4376.
34. Dupré,M., Duchateau,M., Sternke-Hoffmann,R., Boquoi,A., Malosse,C., Fenk,R., Haas,R., Buell,A.K., Rey,M. and Chamot-Rooke,J. (2021) De novo sequencing of antibody light chain proteoforms from patients with multiple myeloma. *Anal. Chem.*, **93**, 10627–10634.
35. Brunet,Y.R., Khodr,A., Logger,L., Aussel,L., Mignot,T., Rimsky,S. and Cascales,E. (2015) H-NS silencing of the Salmonella pathogenicity island 6-encoded type VI secretion system limits *Salmonella enterica* serovar Typhimurium interbacterial killing. *Infect. Immun.*, **83**, 2738–2750.
36. Benz,J., Reinstein,J. and Meinhart,A. (2013) Structural insights into the effector-immunity system Tae4/Tai4 from Salmonella typhimurium. *PLoS One*, **8**, e67362.
37. Sibinelli-Sousa,S., Hespanhol,J.T., Nicastro,G.G., Matsuyama,B.Y., Mesnage,S., Patel,A., de Souza,R.F., Guzzo,C.R. and Bayer-Santos,E. (2020) A family of T6SS antibacterial effectors related to l,d-transpeptidases targets the peptidoglycan. *Cell Rep.*, **31**, 107813.
38. LorenteCobo,N., Sibinelli-Sousa,S., Biboy,J., Vollmer,W., Bayer-Santos,E. and Prehna,G. (2022) Molecular characterization of the type VI secretion system effector Tlde1a reveals a structurally altered LD-transpeptidase fold. *J. Biol. Chem.*, **298**, 102556.
39. Zhang,H., Zhang,H., Gao,Z.-Q., Wang,W.-J., Liu,G.-F., Xu,J.-H., Su,X.-D. and Dong,Y.-H. (2013) Structure of the type VI effector-immunity complex (Tae4-Tai4) provides novel insights into the inhibition mechanism of the effector by its immunity protein. *J. Biol. Chem.*, **288**, 5928–5939.
40. Sana,T.G., Flaugnatti,N., Lugo,K.A., Lam,L.H., Jacobson,A., Baylot,V., Durand,E., Journet,L., Cascales,E. and Monack,D.M. (2016) Salmonella Typhimurium utilizes a T6SS-mediated antibacterial weapon to establish in the host gut. *Proc. Natl Acad. Sci. USA*, **113**, E5044–E5051.
41. Holm,L. (2020) Using Dali for protein structure comparison. *Methods Mol. Biol.*, **2112**, 29–42.
42. Aravind,L., Zhang,D., de Souza,R.F., Anand,S. and Iyer,L.M. (2015) The natural history of ADP-ribosyltransferases and the ADP-ribosylation system. *Curr. Top. Microbiol. Immunol.*, **384**, 3–32.
43. Cohen,M.S. and Chang,P. (2018) Insights into the biogenesis, function, and regulation of ADP-ribosylation. *Nat. Chem. Biol.*, **14**, 236–243.
44. Bazan,J.F. and Koch-Nolte,F. (1997) Sequence and structural links between distant ADP-ribosyltransferase families. *Adv. Exp. Med. Biol.*, **419**, 99–107.
45. Fieldhouse,R.J., Turgeon,Z., White,D. and Merrill,A.R. (2010) Cholera- and anthrax-like toxins are among several new ADP-ribosyltransferases. *PLoS Comput. Biol.*, **6**, e1001029.
46. de Souza,R.F. and Aravind,L. (2012) Identification of novel components of NAD-utilizing metabolic pathways and prediction of their biochemical functions. *Mol. Biosyst.*, **8**, 1661–1677.
47. Jørgensen,R., Wang,Y., Visschedyk,D. and Merrill,A.R. (2008) The nature and character of the transition state for the ADP-ribosyltransferase reaction. *EMBO Rep.*, **9**, 802–809.
48. Ting,S.-Y., Bosch,D.E., Mangiameli,S.M., Radey,M.C., Huang,S., Park,Y.-J., Kelly,K.A., Filip,S.K., Goo,Y.A., Eng,J.K. *et al.* (2018) Bifunctional immunity proteins protect bacteria against FtsZ-targeting ADP-ribosylating toxins. *Cell*, **175**, 1380–1392.
49. Saraste,M., Sibbald,P.R. and Wittinghofer,A. (1990) The P-loop–a common motif in ATP- and GTP-binding proteins. *Trends Biochem. Sci.*, **15**, 430–434.

50. Vetter,I.R. and Wittinghofer,A. (2001) The guanine nucleotide-binding switch in three dimensions. *Science*, **294**, 1299–1304.
51. Jumper,J., Evans,R., Pritzel,A., Green,T., Figurnov,M., Ronneberger,O., Tunyasuvunakool,K., Bates,R., Žídek,A., Potapenko,A. *et al.* (2021) Highly accurate protein structure prediction with AlphaFold. *Nature*, **596**, 583–589.
52. Mirdita,M., Schütze,K., Moriwaki,Y., Heo,L., Ovchinnikov,S. and Steinegger,M. (2022) ColabFold: making protein folding accessible to all. *Nat. Methods*, **19**, 679–682.
53. Abel,K., Yoder,M.D., Hilgenfeld,R. and Jurnak,F. (1996) An alpha to beta conformational switch in EF-Tu. *Structure*, **4**, 1153–1159.
54. Verheugd,P., Bütepage,M., Eckei,L. and Lüscher,B. (2016) Players in ADP-ribosylation: readers and erasers. *Curr. Protein Pept. Sci.*, **17**, 654–667.
55. Deng,Q. and Barbieri,J.T. (2008) Molecular mechanisms of the cytotoxicity of ADP-ribosylating toxins. *Annu. Rev. Microbiol.*, **62**, 271–288.
56. Bulyha,I., Hot,E., Huntley,S. and Søgaard-Andersen,L. (2011) GTPases in bacterial cell polarity and signalling. *Curr. Opin. Microbiol.*, **14**, 726–733.
57. Schweins,T. and Wittinghofer,A. (1994) GTP-binding proteins. Structures, interactions and relationships. *Curr. Biol.*, **4**, 547–550.
58. Wittinghofer,A. and Vetter,I.R. (2011) Structure-function relationships of the G domain, a canonical switch motif. *Annu. Rev. Biochem.*, **80**, 943–971.
59. Aktories,K., Schwan,C. and Jank,T. (2017) Clostridium difficile toxin biology. *Annu. Rev. Microbiol.*, **71**, 281–307.
60. Locht,C., Coutte,L. and Mielcarek,N. (2011) The ins and outs of pertussis toxin. *FEBS J.*, **278**, 4668–4682.
61. Vanden Broeck,D., Horvath,C. and De Wolf,M.J.S. (2007) Vibrio cholerae: cholera toxin. *Int. J. Biochem. Cell Biol.*, **39**, 1771–1775.
62. Iglewski,W.J. (1994) Cellular ADP-ribosylation of elongation factor 2. *Mol. Cell Biochem.*, **138**, 131–133.
63. Wilson,B.A. and Collier,R.J. (1992) Diphtheria toxin and *Pseudomonas aeruginosa* exotoxin A: active-site structure and enzymic mechanism. *Curr. Top Microbiol. Immunol.*, **175**, 27–41.
64. Vyas,S., Matic,I., Uchima,L., Rood,J., Zaja,R., Hay,R.T., Ahel,I. and Chang,P. (2014) Family-wide analysis of poly(ADP-ribose) polymerase activity. *Nat. Commun.*, **5**, 4426.
65. Chaoprasid,P., Lukat,P., Mühlen,S., Heidler,T., Gazdag,E.-M., Dong,S., Bi,W., Rüter,C., Kirchenwitz,M., Steffen,A. *et al.* (2021) Crystal structure of bacterial cytotoxic necrotizing factor CNFY reveals molecular building blocks for intoxication. *EMBO J.*, **40**, e105202.
66. Hoffmann,C., Pop,M., Leemhuis,J., Schirmer,J., Aktories,K. and Schmidt,G. (2004) The Yersinia pseudotuberculosis cytotoxic necrotizing factor (CNFY) selectively activates RhoA. *J. Biol. Chem.*, **279**, 16026–16032.
67. Kato-Murayama,M., Bessho,Y., Shirouzu,M. and Yokoyama,S. (2005) Crystal structure of the RNA 2'-phosphotransferase from Aeropyrum pernix K1. *J. Mol. Biol.*, **348**, 295–305.
68. Maracci,C. and Rodnina,M.V. (2016) Review: translational GTPases. *Biopolymers*, **105**, 463–475.
69. Maracci,C., Peske,F., Dannies,E., Pohl,C. and Rodnina,M.V. (2014) Ribosome-induced tuning of GTP hydrolysis by a translational GTPase. *Proc. Natl Acad. Sci. USA*, **111**, 14418–14423.
70. Kjeldgaard,M. and Nyborg,J. (1992) Refined structure of elongation factor EF-Tu from *Escherichia coli*. *J. Mol. Biol.*, **223**, 721–742.
71. Johansen,J.S., Kavaliauskas,D., Pfeil,S.H., Blaise,M., Cooperman,B.S., Goldman,Y.E., Thirup,S.S. and Knudsen,C.R. (2018) E. coli elongation factor Tu bound to a GTP analogue displays an open conformation equivalent to the GDP-bound form. *Nucleic Acids Res.*, **46**, 8641–8650.
72. Kawashima,T., Berthet-Colominas,C., Wulff,M., Cusack,S. and Leberman,R. (1996) The structure of the *Escherichia coli* EF-Tu.EF-Ts complex at 2.5 A resolution. *Nature*, **379**, 511–518.
73. Wieden,H.-J., Gromadski,K., Rodnin,D. and Rodnina,M.V. (2002) Mechanism of elongation factor (EF)-Ts-catalyzed nucleotide exchange in EF-Tu. Contribution of contacts at the guanine base. *J. Biol. Chem.*, **277**, 6032–6036.
74. Kothe,U., Wieden,H.-J., Mohr,D. and Rodnina,M.V. (2004) Interaction of helix D of elongation factor Tu with helices 4 and 5 of protein L7/12 on the ribosome. *J. Mol. Biol.*, **336**, 1011–1021.